

# Topological magnets and magnons in twisted bilayer MoTe<sub>2</sub> and WSe<sub>2</sub>

Taige Wang,<sup>1,2</sup> Trithep Devakul,<sup>3</sup> Michael P. Zaletel,<sup>1,2</sup> and Liang Fu<sup>3</sup>

<sup>1</sup>*Department of Physics, University of California, Berkeley, CA 94720, USA*

<sup>2</sup>*Material Science Division, Lawrence Berkeley National Laboratory, Berkeley, CA 94720, USA*

<sup>3</sup>*Department of Physics, Massachusetts Institute of Technology, Cambridge, MA 02139 USA*

(Dated: June 21, 2023)

Twisted homobilayer transition metal dichalcogenide (TMD) offers a versatile platform for exploring band topology, interaction-driven phases, and magnetic orders. We study the interaction-driven phases in twisted TMD homobilayers and their low-energy collective excitations, focusing on the effect of band topology on magnetism and its thermal stability. From Hartree-Fock theory of the continuum model, we identify several magnetic and topological phases. By tuning the displacement field, we find two phase transitions involving a change in topology and magnetism respectively. We analyze the magnon spectrum, revealing the crucial role of band topology in stabilizing 2D ferromagnetism by amplifying easy-axis magnetic anisotropy, resulting in a large magnon gap of up to 7 meV. As the magnon gap is directly tied to the stability of the magnetic phase to thermal fluctuations, our findings have several important experimental implications.

*Introduction* – Harnessing the magnetic properties of materials is a long-standing goal in condensed matter physics. In conventional magnets, magnetism is associated with magnetic elements having partially filled  $d$  and  $f$  orbitals, which is difficult to control externally. However, recent experimental breakthroughs in two dimensional moiré heterostructures have opened up new avenues for tailoring magnetism [1, 2]. By tuning control parameters such as twist angle, electrostatic gating, or electric field, it becomes possible to significantly modify the moiré band structure and induce a wide range of interaction-driven states with magnetic orders and topological states. Such interaction-driven magnetism without magnetic elements can even be tuned *in situ* by electrical means. This unprecedented control of magnetism has potential in developing spintronic devices and quantum technologies.

For 2D materials, an important practical question is the stability of these magnetic phases to thermal fluctuations, which is dictated by the nature of low-energy collective modes. Magnetic orders which break a continuous spin rotation symmetry, such as spin  $SU(2)$ , necessarily possess gapless Goldstone modes, generating fluctuations which destroy long range magnetic order in 2D at any finite temperatures by the Mermin-Wagner theorem. Therefore, robust ferromagnetism in 2D requires a large magnetic anisotropy. In pristine graphene systems where spin-orbit coupling is negligibly small, spin ferromagnetism cannot exist as a true long-range order at finite temperature. Even in monolayer TMDs with a strong Ising spin-orbit coupling, the locking of spin  $s_z = \uparrow (\downarrow)$  to valley  $K (K')$  leads to an emergent pseudospin  $SU(2)$  symmetry at low doping, which again suppresses long-range magnetic order. This difficulty is finally overcome in moiré TMD homobilayers, in which the spin-valley locking combined with valley-dependent interlayer tunneling manifestly breaks the pseudospin symmetry down to  $U(1) \times Z_2$  [3], thus enabling true long-

range Ising-type magnetic order at finite temperatures via spontaneous spin  $s_z$  polarization that preserves  $U(1)$  and breaks  $Z_2$  spin symmetry [4]. This is exemplified by recent observations of Ising ferromagnetism, with clear magnetic hysteresis, in twisted homobilayer transition metal dichalcogenide (TMD) at small twist angles [5–7]. Moreover, ferromagnetism combined with non-trivial band topology in TMD bilayer systems may lead to quantized anomalous Hall effect at integer fillings, which has attracted great interest [8–24].

In this work, we study the rich phase space of magnetic orders in twisted TMD homobilayers and their low-energy collective excitations, with a focus on the impact of band topology on magnetism. For twisted homobilayer MoTe<sub>2</sub> and WSe<sub>2</sub> at twist angles  $1^\circ < \theta < 4^\circ$  with realistic interactions, we map out the ground state phase diagram at the filling of one hole per moiré unit cell via self-consistent Hartree-Fock (HF) theory of the continuum model. As a function of twist angle and displacement field, we find a variety of magnetic and topological states, including valley polarized (VP) and inter-valley coherent (IVC) states which exhibit Ising and  $xy$  magnetic orders respectively. We further calculate the spectrum of magnon excitations using the time-dependent HF formalism [25–28].

We show that robust Ising ferromagnetism is directly tied with the presence of topological moiré bands characterized by spin- (equivalently valley-) Chern number. We demonstrate that the band topology stabilizes 2D ferromagnetism by amplifying the easy-axis magnetic anisotropy, resulting in a large magnon gap of up to  $\sim 7$  meV. When a displacement field is applied, we find two transitions in most of the angle range examined. First, the VP state undergoes a topological phase transition from a Chern insulator to a trivial insulator, accompanied by electronic band inversion without change of Ising ferromagnetism. One of our key findings is that across this transition, the magnon

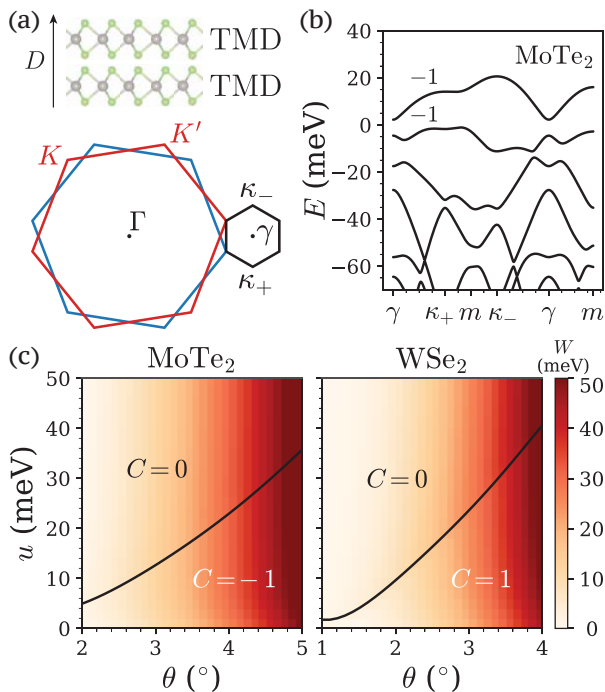


FIG. 1. (a) Atomic structure and Brillouin zone (BZ) of twisted homobilayer TMD. The red and blue BZ are the atomic BZ of the top and the bottom layer respectively, and the black BZ is the resulting moiré BZ. (b) Typical band structure of twisted homobilayer TMD, with twisted MoTe<sub>2</sub> with twist angle  $\theta = 3.5^\circ$  and displacement field  $u_D = 5$  meV as an example. We label the valley Chern numbers of the first two valence bands in the  $K$  valley, which depend on both the twist angle and the displacement field. (c) Band width and valley Chern number of the first valence band in the  $K$  valley as a function of twist angle and displacement field.

gap decreases dramatically, exemplifying the importance of band topology in enhancing magnetic anisotropy. As the displacement field further increases, we find a magnetic phase transition from an Ising ferromagnetic (VP) to an XY antiferromagnetic (IVC) state, which can be understood as the condensation of magnons at a commensurate wave vector. This corresponds to a continuous magnetic canting transition across which the charge gap does not close.

*Continuum model* – In twisted TMDs, the valence band edge is located at the  $K$  and  $K'$  point of the Brillouin zone [4, 29]. The strong Ising spin-orbit coupling locks the spin degree of freedom to the valley degree of freedom at low energy. Following Ref. 3, we write down the continuum model Hamiltonian,

$$H_0 = \sum_{\tau,l,r} c_{\tau,l,r}^\dagger ([h_\tau]_{ll'} - \mu\delta_{ll'}) c_{\tau,l',r} \quad (1)$$

$$[h_K]_{ll'} = \begin{pmatrix} h_+^K + V_+(\mathbf{r}) + u_D & T(\mathbf{r}) \\ T^\dagger(\mathbf{r}) & h_-^K + V_-(\mathbf{r}) - u_D \end{pmatrix}$$

where  $\tau$  is the valley index and  $l$  is the layer index. Here  $h_\pm^K$  is the kinetic part,  $V_\pm(\mathbf{r})$  and  $T(\mathbf{r})$  are the intralayer

moiré potential and interlayer tunneling respectively due to the moiré structure. In the Supplementary Material [30], we give the explicit form of  $V_\pm(\mathbf{r})$  and  $T(\mathbf{r})$ , and the continuum model parameters from recent large-scale DFT calculations [4, 29]. A vertical displacement field is modeled as a layer potential difference  $u_D$ . The  $K'$  valley hamiltonian  $h_{K'}$  can be obtained as the time-reversal conjugate of  $h_K$ .

In addition to the moiré point group symmetries, i.e., the translation  $T_{1,2}$  and the threefold rotation  $C_3$  symmetry, the twisted TMD Hamiltonian in Eqn. 1 also respects the total charge  $U(1)_c$ , the valley charge  $U(1)_v$ , and the time reversal symmetry  $\mathcal{T}$ . We typically consider finite vertical displacement fields which breaks the  $C_{2y}$  rotation symmetry at  $u_D = 0$ .

The typical non-interacting band structure of twisted TMD is shown in Fig. 1 (b). We calculate the bandwidth and the valley Chern number of the first valence band for twisted MoTe<sub>2</sub> and WSe<sub>2</sub> at various twist angles and displacement fields, shown in Fig. 1 (c). At zero displacement field, twisted WSe<sub>2</sub> has valley Chern number  $C_K = 1$  and twisted MoTe<sub>2</sub> has  $C_K = -1$  [29]. The valley Chern number vanishes beyond a critical displacement field  $u_D^c$ , which depends on the twist angle. As we will now show, the twist angle and the tunable valley Chern number have a profound influence on the interaction-driven phases.

*Interaction-driven phases* – Now we examine the effect of interaction by adding a gated screened Coulomb interaction to the Hamiltonian. We study the interacting Hamiltonian with band-projected self-consistent Hartree-Fock numerics, as detailed in the Supplementary Material [30]. As shown in Fig. 2 (a), we observe a rich interacting phase diagram at one hole per moiré unit cell that features various magnetic orders. For realistic dielectric constant  $\epsilon < 25$ , we always observe an incompressible state that breaks various combinations of the valley  $U(1)_v$  symmetry and the time reversal  $\mathcal{T}$  symmetry [30]. Here we restrict ourselves to two *active* bands per valley, which gives most robust results against small perturbations in the continuum model parameters. We remark that the third band can affect parts of the phase diagram of twisted MoTe<sub>2</sub> in a way which sensitively depends on the phase of the moiré potential (see Supplementary Material for a detailed discussion).

The prominent states in play are the valley polarized (VP) state, inter-valley coherent (IVC) state at zero momentum (IVC<sub>0</sub>), and IVC state at momentum  $\mathbf{Q} = \kappa_+ - \kappa_- = \kappa_-$  (IVC<sub>Q</sub>) (see Fig. 1 (a)). Due to spin-valley locking, the VP state is an Ising ferromagnet with out-of-plane spin polarization. The IVC states show three-sublattice 120° antiferromagnetic order at atomic scale. The order parameter can be represented as a complex scalar field  $S^+ \equiv S_x + iS_y$  and we label its moiré scale momentum  $\mathbf{q} \ll K$ ,

$$S_{\text{IVC}}^+(\mathbf{q}) = \sum_{\mathbf{r}} e^{-i(\mathbf{K}' - \mathbf{K} + \mathbf{q}) \cdot \mathbf{r}} S^+(\mathbf{r}) \sim \sum_{\mathbf{k}} \langle \psi_{K,\mathbf{k}}^\dagger \psi_{K',\mathbf{k} + \mathbf{q}} \rangle \quad (2)$$

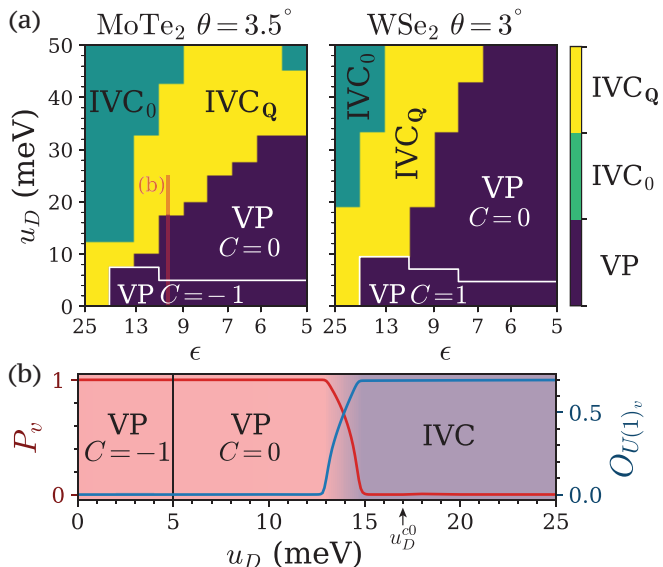


FIG. 2. (a) Interacting phase diagram of twisted MoTe<sub>2</sub> and WSe<sub>2</sub> as a function of displacement field and dielectric constant. Different colors represent three different phases: VP, IVC<sub>0</sub>, and IVC<sub>Q</sub> (see main text for definition). We label the regime where the ground state has non-zero Chern number. (b) Typical phase transition as a function of displacement field following the red line cut in (a) ( $\epsilon = 10$ ). We show the valley polarization  $P_v$  and the order parameter of  $U(1)_v$  symmetry breaking (see main text for definition). We also remark the displacement field  $u_D^c$  at which the valley Chern number of the non-interacting band vanishes.

where  $\psi_{\tau,\mathbf{k}}^\dagger$  denotes the moiré Bloch electrons of the  $\tau$  valley.

The IVC state with  $\mathbf{q} = 0$  preserves the translational symmetry of the moiré superlattice, while the one with the commensurate wavevector  $\mathbf{Q}$  triples the unit cell and the AFM order parameter forms a spiral at moiré scale. The magnetic orders of various valley-ordered states are summarized in Table I.

Magnetic orders	Valley-ordered phases
QAH	topological VP
FM <sub>z</sub>	trivial VP
FM <sub>xy</sub>	IVC <sub>0</sub>
120° AFM	IVC <sub>Q</sub>

TABLE I. Magnetism and topology of various valley-ordered states.

Both topological and non-topological VP phases exist in the phase diagram of Fig. 2 (a). We remark that the topological trivial VP phase is adiabatically connected to the multiferroic phase discussed in Ref. 21, which survives down to zero displacement field at small twist angles (see Fig. 3 (a)).

Now we discuss the phase transition between these interaction-driven phases. The most relevant tuning knob in the experiment is the displacement field, which

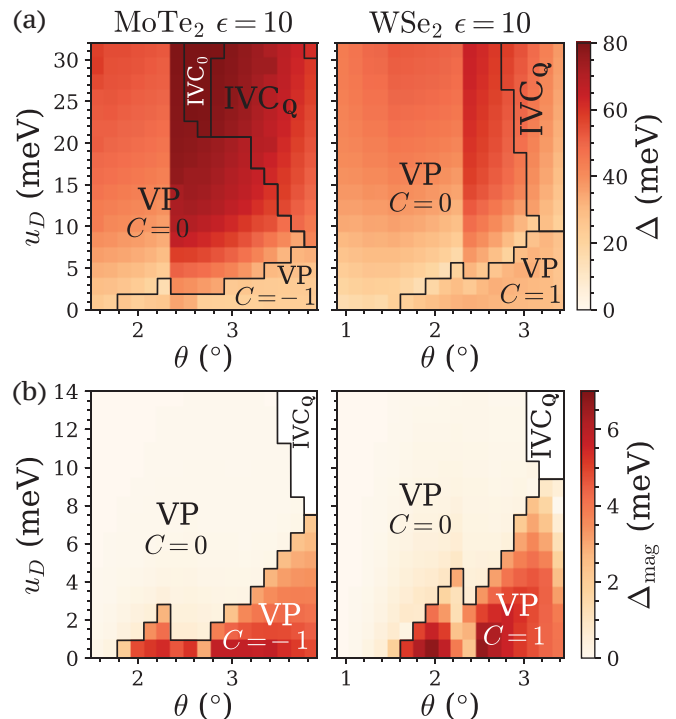


FIG. 3. Interacting phase diagram of twisted MoTe<sub>2</sub> and WSe<sub>2</sub> as a function of displacement field and twist angle. We show the charge gap in (a) and the magnon gap in (b). The IVC phase has gapless Goldstone modes instead of magnons, which is left blank in (b). We note that the magnon gap is non-vanishing, but parametrically small in the regime where the VP state is topologically trivial.

can already tune among all magnetic orders discussed above at suitable twist angle. We show the evolution of various order parameters as a function of displacement field  $u_D$  in Fig. 2 (b) at some generic twist angle  $\theta = 3.5^\circ$  and dielectric constant  $\epsilon = 10$  (shown as the red line cut in Fig. 2 (a)). At small  $u_D$ , the large gap between the first two valence bands prevents the interaction from mixing the two bands. Therefore, it is energetically favorable to fill the first valence band of one valley, resulting in a topological  $C = \pm 1$  VP state inheriting the Chern number from the noninteracting band. At some critical  $u_D^c$ , which is much smaller than in the non-interacting case  $u_D^c$ , the bulk gap closes and the VP state transitions into a topologically trivial VP state. Then at a larger  $u_D \gg u_D^c$ , there is a second transition at which the VP state smoothly cants into an IVC state on the valley Bloch sphere without the bulk gap closing [31]. In Fig. 2 (b), we can see how the valley polarization  $P_v \equiv (n_K - n_{K'}) / (n_K + n_{K'})$  smoothly vanishes and the  $U(1)_v$  symmetry breaking  $O_{U(1)_v} \equiv \sum_{\mathbf{k}} |\langle \psi_{K,\mathbf{k}}^\dagger \psi_{K',\mathbf{k}} \rangle|$  smoothly turns on across a displacement field range of 2 meV. Here,  $n_\tau \sim \sum_{\mathbf{k}} \langle \psi_{\tau,\mathbf{k}}^\dagger \psi_{\tau,\mathbf{k}} \rangle$  is the occupation of the  $\tau$  valley.

In Fig. 3, we show the phase diagram at fixed dielectric constant  $\epsilon = 10$  while varying twist angle

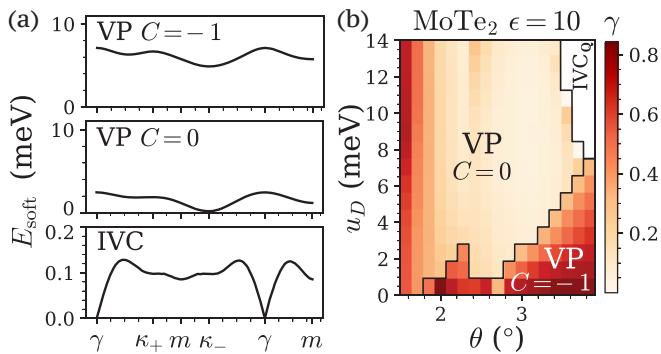


FIG. 4. (a) Typical soft mode band structure of twisted TMD in the topological VP, trivial VP and the IVC phase. We take twisted MoTe<sub>2</sub> with  $\theta = 3.5^\circ$  at  $u_D = 1.2$  meV (topological VP), 5 meV (trivial VP), and 20 meV (IVC) as an example. (b) Ising anisotropy as a function of displacement field and twist angle (see main text for definition).

and displacement field. The charge gap can be directly compared with transport experiments. As the twist angle increases, the critical displacement field  $u_D^c$  for the topological transition also increases, following the trend of noninteracting  $u_D^c$ . Such resemblance can be understood as  $u_D^c$  being the displacement field required to fully close the gap between the first two valence bands, while  $u_D$  being the field required to bring the gap down the interaction energy scale such that interaction can mix these two bands. Generally, interactions will tend to increase the layer polarization, resulting in a topologically trivial band.

On the other hand, as the twist angle increases, the second magnetic transition into the IVC state occurs at reduced  $u_D$ . The IVC state can benefit from the more dispersive bands at larger twist angles by canting the valley isospin vector in momentum space [32–34]. Therefore, at large enough twist angle, the intermediate trivial VP phase disappears (see Fig. 3 (a)), and the topological transition and the magnetic transition merge into a single transition (see the Supplementary Materials for more details) [30]. A canting-induced topological transition between  $C = 1$  and  $C = 0$  magnetic states can be described by the theory of charge transfer gap inversion [11].

*Magnon and thermal stability of the magnetic orders* – Now we discuss the finite-temperature stability of these magnetic orders, which is controlled by the low energy collective modes. More precisely, thermal fluctuation of these modes, present at temperatures higher than their gap, leads to melting of the magnetic order. We employ the time-dependent HF calculation [26–28], as implemented for moiré heterostructures in Ref. 25, to compute all soft mode excitations in the HF ground state.

We show the magnon band of twisted MoTe<sub>2</sub> at  $\theta = 3.5^\circ$  in Fig. 4 as an example. In the topological VP phase, the magnon band is relatively flat and features a large magnon gap. Once we cross the

transition into the trivial VP phase, the magnon gap drops significantly despite a similar magnon bandwidth. Here, we see the prototypical (almost) gapless quadratic Goldstone modes of a (nearly) isotropic ferromagnet (the pseudospin  $SU(2)$  rotation symmetry becomes exact in our model when  $u_D \rightarrow \infty$ , which reduces to a monolayer with a periodic potential). When we finally reach the IVC<sub>Q</sub> phase, the low energy soft modes are no longer magnons that carry spin quantum number. Instead, we find linearly dispersed gapless goldstone modes from spontaneously breaking of the valley  $U(1)_v$  symmetry.

Fig. 3 (b) emphasizes the correlation between the non-trivial band topology and the magnon gap. The magnon gap can reach up to  $\sim 7$  meV in the topological VP phase, while it quickly drops to almost zero across the topological transition. This behavior requires understanding the nature of the low-energy soft modes. In the VP phase (topological or not), we find that the soft mode at the magnon band bottom corresponds to a spin-valley flip with momentum moiré momentum  $\mathbf{Q} = \kappa_-$ ,

$$|m(\mathbf{Q})\rangle \sim \sum_{\mathbf{k}} \psi_{K,\mathbf{k}}^\dagger \psi_{K',\mathbf{k}+\mathbf{Q}} |\text{VP}\rangle \quad (3)$$

We note that condensing such a magnon will result in an IVC state with momentum  $\mathbf{Q}$ , which is characterized by  $S_{\text{IVC}}^+ \sim \sum_{\mathbf{k}} \langle \psi_{K,\mathbf{k}}^\dagger \psi_{K',\mathbf{k}+\mathbf{q}} \rangle$ . The IVC state can be viewed as a coherent superposition of the first valence bands of the two valleys. When those two bands carry nonzero and opposite Chern number, the phase of the IVC order parameter necessarily winds non-trivially in the momentum space, which results in an additional energy cost relative to the VP state [34–39]. Therefore, when the parent state is a topological VP state, the additional energy required to condense into the IVC state, or the magnon gap, is higher.

Alternatively, the energy difference between the VP and the IVC state signifies the spin-valley  $SU(2)$  breaking. As an analogy, consider the ferromagnetic Heisenberg model, in which the spin anisotropy dictates the magnon gap, we can similarly define the Ising anisotropy  $\gamma = \Delta_{\text{mag}} / (\Delta_{\text{mag}} + W_{\text{mag}})$  with  $\Delta_{\text{mag}}$  being the magnon gap and  $W_{\text{mag}}$  being the magnon band width. We show  $\gamma$  as a function of the twist angle and the displacement field in Fig. 4 (b), which drops across the topological transition. The correspondence between the VP and IVC energy difference and the magnetic anisotropy also implies a larger magnon gap and therefore a more stable magnetism at larger twist angles, at which the IVC state is more energetically favorable. In addition, nontrivial topology forces the electron wave function to be more spread out, and thereby enhances the exchange interaction that relies on the wave function overlap. The combined effect of increased magnetic anisotropy and exchange interaction enhances Ising ferromagnetism when the underlying electronic band is topologically non-trivial.

*Discussion* – Our result that topology strongly enhances the magnetic anisotropy, and hence the magnon

gap and Curie temperature, has important implications for previous studies. Previously obtained interaction-driven phase diagrams of TMD homobilayers [4, 17, 18, 21, 24], using a variety of different theoretical techniques and models, find qualitatively similar candidates of magnetic and topological phases including topological and non-topological VP ferromagnets. However, the displacement-field-induced phase transitions observed here and the unique physics at larger twist angles have not been previously discussed. While previous studies did not analyze the magnon spectrum, our results predict that the topological ferromagnets are dramatically more robust to thermal fluctuations than their nontopological counterparts.

In this study, we have analyzed the different magnetic orders, their tunability, and thermal stability in twisted TMD. Our results make several testable predictions for future experimental studies. By increasing the vertical displacement field, it is possible to sequentially transition from the topological VP state to the trivial VP state, and finally to the IVC state, as depicted in Fig. 2 (b). A displacement field tuned transition from VP to a non-VP phase has recently been observed [5] consistent with our theory, and our analyses reveal several new aspects. Namely, we predict that this progression involves two key transitions. The first topological transition from the topological VP state to the trivial VP state can be investigated using transport experiments that measure the quantized Hall conductance. The second soft canting transition from the trivial VP state to the IVC state can be directly observed optically via magnetic circular dichroism (MCD), which probes the degree of valley polarization.

Our theory shows that the ferromagnetic ordering temperature is strongly affected by the topology of the electronic states. In the topologically trivial VP phase, the long-range ferromagnetic order is suppressed

at finite temperature due to an approximate SU(2) symmetry; a concrete prediction is that the ordering temperature, as indicated by magnetic hysteresis, is much lower than the Curie-Weiss temperature obtained from fitting magnetic susceptibility at high temperatures. This result emphasizes the physical significance of the magnon spectrum: despite the large charge gap observed in TMDs, the magnetic ordering temperatures are significantly lower as they are controlled by the magnon gap. Therefore, our work serves to guide the search for highly tunable robust ferromagnetic states in the moiré platform.

*Note added.* After we post this manuscript, we become aware of a preprint that studies twisted MoTe<sub>2</sub> at  $\theta = 3.7^\circ$  using self-consistent Hartree Fock and density matrix renormalization group (DMRG) numerics, which agrees with our phase diagram at  $\theta = 3.7^\circ$  [40].

#### ACKNOWLEDGMENTS

We thank Xiaodong Xu, Shubhayu Chatterjee, and Tomohiro Soejima for helpful discussions. We thank Nick Bultinck and Tomohiro Soejima for their contributions to the code used to perform the HF and TDHF calculations. We thank Yang Zhang for providing the TMD atomic structure figure. This work was supported by the Air Force Office of Scientific Research (AFOSR) under award FA9550-22-1-0432 (TD and LF), and the U.S. Department of Energy, Office of Science, Office of Basic Energy Sciences, Materials Sciences and Engineering Division under Contract No. DE-AC02-05-CH11231 (van der Waals Heterostructures Program KCWF16) (TW and MZ). This research used the Lawrence computational cluster resource provided by the IT Division at the Lawrence Berkeley National Laboratory (Supported by the Director, Office of Science, Office of Basic Energy Sciences, of the U.S. Department of Energy under Contract No. DE-AC02-05CH11231).

- 
- [1] E. Y. Andrei, D. K. Efetov, P. Jarillo-Herrero, A. H. MacDonald, K. F. Mak, T. Senthil, E. Tutuc, A. Yazdani, and A. F. Young, *Nature Reviews Materials* **6**, 201 (2021).
  - [2] K. F. Mak and J. Shan, *Nature Nanotechnology* **17**, 686 (2022).
  - [3] F. Wu, T. Lovorn, E. Tutuc, I. Martin, and A. H. MacDonald, *Phys. Rev. Lett.* **122**, 086402 (2019).
  - [4] T. Devakul, V. Crépel, Y. Zhang, and L. Fu, *Nature Communications* **12**, 6730 (2021).
  - [5] E. Anderson, F.-R. Fan, J. Cai, W. Holtzmann, T. Taniguchi, K. Watanabe, D. Xiao, W. Yao, and X. Xu, (2023), arXiv:2303.17038 [cond-mat.mes-hall].
  - [6] J. Cai, E. Anderson, C. Wang, X. Zhang, X. Liu, W. Holtzmann, Y. Zhang, F. Fan, T. Taniguchi, K. Watanabe, Y. Ran, T. Cao, L. Fu, D. Xiao, W. Yao, and X. Xu, (2023), arXiv:2304.08470 [cond-mat.mes-hall].
  - [7] Y. Zeng, Z. Xia, K. Kang, J. Zhu, P. Knüppel, C. Vaswani, K. Watanabe, T. Taniguchi, K. F. Mak, and J. Shan, arXiv preprint arXiv:2305.00973 (2023).
  - [8] T. Li, S. Jiang, B. Shen, Y. Zhang, L. Li, Z. Tao, T. Devakul, K. Watanabe, T. Taniguchi, L. Fu, *et al.*, *Nature* **600**, 641 (2021).
  - [9] B. A. Foutty, C. R. Kometter, T. Devakul, A. P. Reddy, K. Watanabe, T. Taniguchi, L. Fu, and B. E. Feldman, (2023), arXiv:2304.09808 [cond-mat.mes-hall].
  - [10] L. Wang, E.-M. Shih, A. Ghiotto, L. Xian, D. A. Rhodes, C. Tan, M. Claassen, D. M. Kennes, Y. Bai, B. Kim, *et al.*, *Nature materials* **19**, 861 (2020).
  - [11] T. Devakul and L. Fu, *Phys. Rev. X* **12**, 021031 (2022).
  - [12] H. Pan, M. Xie, F. Wu, and S. D. Sarma, *Physical Review Letters* **129**, 056804 (2022).
  - [13] Y.-M. Xie, C.-P. Zhang, J.-X. Hu, K. F. Mak, and K. T. Law, *Physical Review Letters* **128**, 026402 (2022).
  - [14] Y.-M. Xie, C.-P. Zhang, and K. Law, arXiv preprint arXiv:2206.11666 (2022).
  - [15] Z. Dong and Y.-H. Zhang, *Physical Review B* **107**,

- L081101 (2023).
- [16] Y.-W. Chang and Y.-C. Chang, Physical Review B **106**, 245412 (2022).
- [17] H. Pan, F. Wu, and S. D. Sarma, Physical Review Research **2**, 033087 (2020).
- [18] J. Zang, J. Wang, J. Cano, and A. J. Millis, Physical Review B **104**, 075150 (2021).
- [19] P. Mai, J. Zhao, B. E. Feldman, and P. W. Phillips, arXiv preprint arXiv:2210.11486 (2022).
- [20] M. Xie, H. Pan, F. Wu, and S. D. Sarma, arXiv preprint arXiv:2206.12427 (2022).
- [21] A. Abouelkomsan, E. J. Bergholtz, and S. Chatterjee, (2022), arXiv:2210.14918 [cond-mat.str-el].
- [22] S. Patra, P. Boyal, and P. Mahadevan, Physical Review B **107**, L041104 (2023).
- [23] S. Ryee and T. O. Wehling, Nano Letters (2023).
- [24] W.-X. Qiu, B. Li, X.-J. Luo, and F. Wu, arXiv preprint arXiv:2305.01006 (2023).
- [25] E. Khalaf, N. Bultinck, A. Vishwanath, and M. P. Zaletel, (2020), arXiv:2009.14827 [cond-mat.str-el].
- [26] F. Wu and S. D. Sarma, Physical Review B **101**, 155149 (2020).
- [27] F. Wu and S. D. Sarma, Physical review letters **124**, 046403 (2020).
- [28] Y. H. Kwan, Y. Hu, S. H. Simon, and S. Parameswaran, Physical Review Letters **126**, 137601 (2021).
- [29] A. P. Reddy, F. F. Alsallom, Y. Zhang, T. Devakul, and L. Fu, (2023), arXiv:2304.12261 [cond-mat.mes-hall].
- [30] For more details see the Supplementary Information.
- [31] N. Bultinck, E. Khalaf, S. Liu, S. Chatterjee, A. Vishwanath, and M. P. Zaletel, Phys. Rev. X **10**, 031034 (2020).
- [32] H. C. Po, L. Zou, A. Vishwanath, and T. Senthil, Phys. Rev. X **8**, 031089 (2018).
- [33] J. Y. Lee, E. Khalaf, S. Liu, X. Liu, Z. Hao, P. Kim, and A. Vishwanath, Nature Communications **10**, 5333 (2019).
- [34] S. Chatterjee, T. Wang, E. Berg, and M. P. Zaletel, Nature Communications **13**, 6013 (2022).
- [35] N. Bultinck, S. Chatterjee, and M. P. Zaletel, Physical Review Letters **124** (2020), 10.1103/physrevlett.124.166601.
- [36] A. L. Sharpe, E. J. Fox, A. W. Barnard, J. Finney, K. Watanabe, T. Taniguchi, M. A. Kastner, and D. Goldhaber-Gordon, Science **365**, 605 (2019).
- [37] M. Serlin, C. L. Tschirhart, H. Polshyn, Y. Zhang, J. Zhu, K. Watanabe, T. Taniguchi, L. Balents, and A. F. Young, Science **367**, 900–903 (2019).
- [38] Y.-H. Zhang, D. Mao, and T. Senthil, Physical Review Research **1** (2019), 10.1103/physrevresearch.1.033126.
- [39] N. Bultinck, E. Khalaf, S. Liu, S. Chatterjee, A. Vishwanath, and M. P. Zaletel, Phys. Rev. X **10**, 031034 (2020).
- [40] J. Dong, J. Wang, P. J. Ledwith, A. Vishwanath, and D. E. Parker, (2023), arXiv:2306.01719 [cond-mat.str-el].
- [41] K. N. Kudin, G. E. Scuseria, and E. Cancès, The Journal of Chemical Physics **116**, 8255 (2002).
- [42] E. Cancès and C. Le Bris, International Journal of Quantum Chemistry **79**, 82.
- [43] Here we take the energy of IVC<sub>0</sub> to represent the energy of generic IVC states.

## Supplemental Material: Topological magnets and magnons in twisted bilayer MoTe<sub>2</sub> and WSe<sub>2</sub>

### SI. CONTINUUM MODEL OF TWISTED TMDS

In the main text, we write down the continuum model Hamiltonian of twisted TMD,

$$H_0 = \sum_{\tau,l,\mathbf{r}} c_{\tau,l,\mathbf{r}}^\dagger ([h_\tau]_{ll'} - \mu\delta_{ll'}) c_{\tau,l,\mathbf{r}}, \quad [h_K]_{ll'} = \begin{pmatrix} h_+^K + V_+(\mathbf{r}) + u_D & T(\mathbf{r}) \\ T^\dagger(\mathbf{r}) & h_-^K + V_-(\mathbf{r}) - u_D \end{pmatrix} \quad (S1)$$

where  $\tau$  is the valley index and  $l$  is the layer index. The kinetic part  $h_\pm^K$  takes the form

$$h_\pm^K = -\frac{\hbar^2 (-i\nabla - \kappa_\pm)^2}{2m^*} \quad (S2)$$

where  $m^*$  is the effective mass. Here  $\kappa_+$  and  $\kappa_-$  are the  $K$  points of the top and bottom layer respectively, which got folded to the moiré Brillouin zone corners (see Fig. 2 (a)). The moiré structure results in an intralayer moiré potential,

$$V_\pm(\mathbf{r}) = 2V \sum_{j=1,3,5} \cos(\mathbf{g}_j \cdot \mathbf{r} \pm \phi) \quad (S3)$$

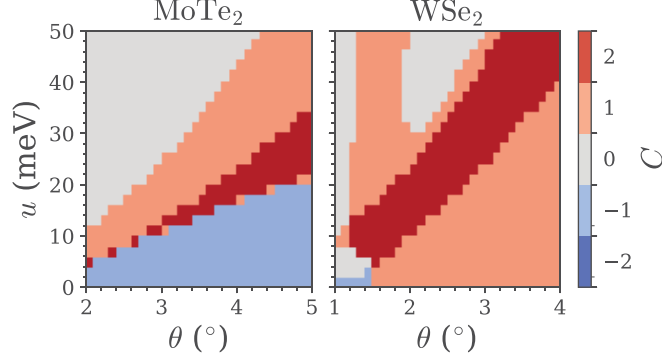
and an interlayer tunneling,

$$T(\mathbf{r}) = w (1 + e^{-i\mathbf{g}_2 \cdot \mathbf{r}} + e^{-i\mathbf{g}_3 \cdot \mathbf{r}}) \quad (S4)$$

where  $\mathbf{g}_j = \frac{4\pi}{\sqrt{3}a_M} (\cos \frac{\pi(j-1)}{3}, \sin \frac{\pi(j-1)}{3})$  are the moiré reciprocal lattice vectors. Here  $a_M = \frac{a_0}{2 \sin(\theta/2)}$  is the moiré lattice constant, with  $\theta$  being the twist angle and  $a_0$  being the atomic lattice constant. Here we write down the  $K$

Materials	$\phi$ ( $^\circ$ )	$V$ (meV)	$w$ (meV)	$m^*$ ( $m_e$ )	$a_0$ ( $\text{\AA}$ )
MoTe <sub>2</sub>	-91	11.2	-13.3	0.62	3.47
WSe <sub>2</sub>	128	9	18	0.43	3.32

TABLE SI. Continuum model parameters of twisted TMDs.

FIG. S1. Valley Chern number of the *second* valence band in the *K* valley as a function of twist angle and displacement field.

valley Hamiltonian  $h_K$  explicitly, while  $h_{K'}$  can be obtained as the time-reversal conjugate of  $h_K$ . In this work, we use continuum model parameters obtained from recent large scale DFT calculations, see Table SI [4, 29].

In the main text, we present the bandwidth and the valley Chern number of the first valence band (see Fig. 1 (c)). Now we will briefly discuss the valley Chern number of the second valence band. As shown in Fig. S1, the valley Chern number has a complicated dependence on both the twist angle  $\theta$  and the displacement field  $u_D$ . We note that at parameter regime where the first valence band is topological, the valley Chern number of the second valence band is the same as the first valence band. Therefore, simply including both bands does not admit any tight-binding description in the parameter regime of interest. In the interaction-driven trivial VP phase, the second valence band usually acquires higher Chern number so that the filled first valence band can be trivial.

## SII. INTERACTING HAMILTONIAN AND INTERACTION-DRIVEN PHASES

### A. Interacting Hamiltonian and self-consistent Hartree-Fock (HF) numerics

Now we introduce the interacting Hamiltonian,

$$H = H_0 + H_C, \quad H_C = \frac{1}{2A} \sum_{\mathbf{q}} V_C(\mathbf{q}) : \rho(\mathbf{q}) \rho(-\mathbf{q}) : \quad (\text{S5})$$

where  $A$  is the sample area,  $V_C(\mathbf{q}) = e^2 \tanh(qD)/(2\epsilon q)$  is the repulsive dual gate screened Coulomb interaction with sample-gate distance  $D = 30$  nm, and  $\rho(\mathbf{q})$  is the Fourier transform of the electron density operator  $\rho(\mathbf{r}) = \sum_{\tau, l, \mathbf{r}} c_{\tau, l, \mathbf{r}}^\dagger c_{\tau, l, \mathbf{r}}$ . Here we neglect any intervalley Hund's coupling that could either come from Coulomb interaction or phonon-induced coupling. We emphasize that the magnetic anisotropy we focus on in this work is induced by the kinetic energy, even in the absence of any intervalley Hund's coupling. For future convenience, we introduce the moiré Bloch electron operator  $\psi_{n, \tau, \mathbf{k}}^\dagger = \sum_l u_{n, \tau, l, \mathbf{k}}^* c_{\tau, l, \mathbf{k}}^\dagger$  with  $u_{n, \tau, l, \mathbf{k}}^*$  being the Bloch wave functions and  $n$  being the band index. The  $\psi_{\tau, \mathbf{k}}^\dagger$  operator introduced in the main text is defined to sum over all bands,  $\psi_{\tau, \mathbf{k}}^\dagger \equiv \sum_n \psi_{n, \tau, \mathbf{k}}^\dagger$ . Now we can also write the density operator in terms of the intravalley form factor  $\rho(\mathbf{q}) = \sum_{\tau, \mathbf{k}, nn'} [\lambda_{\mathbf{q}}^{\tau\tau}(\mathbf{k})]^{n'n} \psi_{n, \tau, \mathbf{k}}^\dagger \psi_{n', \tau, \mathbf{k}+\mathbf{q}}$  where  $[\lambda_{\mathbf{q}}^{\tau\tau}(\mathbf{k})]^{n'n} = \langle u_{n, \tau, \mathbf{k}} | u_{n', \tau', \mathbf{k}+\mathbf{q}} \rangle$ .

We study this interacting Hamiltonian using a self-consistent Hartree-Fock (HF) calculation. To reduce the computational cost, we project the Coulomb interaction to the first two valence bands per valley, which allows us to use a  $30 \times 30$  momentum grid to efficiently sweep the phase diagram and a  $60 \times 60$  momentum grid to extract HF band structures. Keeping at least two bands per valley is essential at filling one hole per moiré unit cell since it allows an interaction-induced topological transition by mixing multiple bands, which plays an essential role in our study of magnetic orders and their magnetic anisotropy. Later, we will also justify that keeping two bands is sufficient

for most quantities of interest. We note that the projected Hamiltonian does not admit any tight-binding description even after involving multiple bands since the net valley Chern number of these bands is still not necessarily vanishing.

Using the formulation described in Ref. 39, we solve the self-consistent equations for Slater determinant states characterized by the one-electron covariance matrix,

$$[P_{\mathbf{Q}}^{\tau'\tau}]^{n'n}(\mathbf{k}) = \begin{cases} \langle \psi_{n,\tau,\mathbf{k}}^\dagger \psi_{n',\tau',\mathbf{k}} \rangle, & \tau = \tau' \\ \langle \psi_{n,\tau,\mathbf{k}}^\dagger \psi_{n',-\tau',\mathbf{k}+\mathbf{Q}} \rangle, & \tau = -\tau' \end{cases} \quad (\text{S6})$$

where we allow a shift  $\mathbf{Q}$  for any intervalley coherence [9]. Then we use both the ODA and the EDIIS algorithms to solve the self-consistency equation [41, 42]. In general, we should allow all possible  $\mathbf{Q}$  at the same time  $P[\{\mathbf{Q}\}]$ , but in this work we will focus on those states characterized by a single  $\mathbf{Q}_0$ , i.e.  $P[\{\mathbf{Q}\}] = \delta_{\mathbf{Q},\mathbf{Q}_0} P_{\mathbf{Q}_0}$ . We always find the lowest energy ground state to be realized when  $\mathbf{Q}$  coincides with high-symmetry points  $\mathbf{Q} = \mathbf{0}$  and  $\mathbf{Q} = \kappa_-$  in the parameter space we study. We note that  $\mathbf{Q} = \kappa_+$  and  $\mathbf{Q} = \kappa_-$  are not equivalent since the displacement field breaks the  $C_{2y}$  rotation symmetry that relates the two.

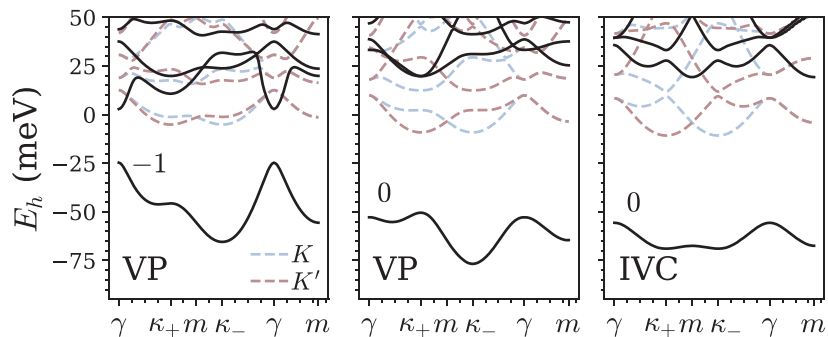


FIG. S2. Typical HF band structure of twisted TMD in the topological VP, trivial VP and the IVC phase. We take twisted MoTe<sub>2</sub> with  $\theta = 3.5^\circ$  at  $u_D = 3$  meV ( $C = -1$  VP), 9 meV ( $C = 0$  VP), and 20 meV (IVC <sub>$\mathbf{Q}$</sub> ) as examples. Here we show the hole energy spectrum, so the electron valence bands in Fig. 1 (b) becomes hole conduction bands here. We label the Chern number of the first HF hole conduction band. We overlay the free hole band structure of both valleys at the corresponding parameters in dashed lines. For VP phases we always plot the HF band structure when the state polarizes to the  $K$  valley.

## B. Interaction-driven phases and their HF band structures

Magnetic orders	Valley-ordered phases	Symmetry Topology		
		$\tilde{\mathcal{T}}$	$U(1)_v$	$C$
/	SM	✓	✓	0
QAH	topological VP	×	✓	$\pm 1$
FM <sub><math>z</math></sub>	trivial VP	×	✓	0
FM <sub><math>xy</math></sub>	IVC <sub><math>\mathbf{0}</math></sub>	✓	×	0
120° AFM	IVC <sub><math>\mathbf{Q}</math></sub>	✓	×	0

TABLE SII. Symmetry and topology of various valley-ordered states. Here  $\tilde{\mathcal{T}}$  is time-reversal combined with 180° spin rotation.

We start with how we identify different phases in HF. Depending on which symmetries are explicitly enforced, we can find three self-consistent solutions: (i) a valley polarized (VP) state which breaks the  $\tilde{\mathcal{T}} = \mathcal{T}e^{i\pi s^z}$  symmetry (time-reversal combined with 180° spin rotation around the  $z$  axis [11]) but preserves the valley  $U(1)_v$  symmetry, (ii) a inter-valley coherent (IVC) state which breaks  $U(1)_v$  symmetry but preserves the  $\tilde{\mathcal{T}}$  symmetry, and (iii) a fully symmetric metal (SM) that respects both of the symmetries (see Table SII). When we study transition between VP and IVC, we allow both  $\tilde{\mathcal{T}}$  and  $U(1)_v$  breaking, which is necessary to capture the smooth canting transition from trivial VP to IVC. We only find SM to be favorable under an unrealistically large dielectric  $\epsilon > 50$  in the parameter regime of interest. We further distinguish the topological VP phase and the trivial VP phase by computing the Chern

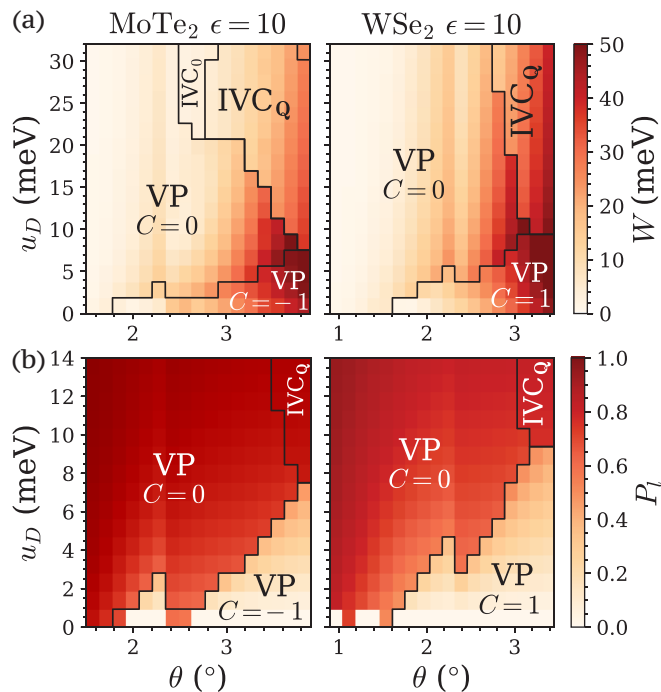


FIG. S3. Interacting phase diagram of twisted MoTe<sub>2</sub> and WSe<sub>2</sub> as a function of displacement field and twist angle. We show the renormalized band width  $W$  in (a) and the layer polarization  $P_l$  in (b). Here  $P_l \equiv (n_t - n_b)/(n_t + n_b)$ ,  $n_l \sim \sum_{\mathbf{k}} \langle c_{l,\mathbf{k}}^\dagger c_{l,\mathbf{k}} \rangle$  is the occupation of the  $l$  layer, and  $c_{l,\mathbf{k}}^\dagger \equiv \sum_{\tau} c_{\tau,l,\mathbf{k}}^\dagger$ .

number of the filled first HF valence band. The momentum shift  $\mathbf{Q}$  in the intervalley sector is irrelevant to the VP phase whose covariance matrix only has intravalley components. However, IVC state with different momentum shift  $\mathbf{Q}$  can have different energy. We always find IVC state with momentum shift  $\mathbf{Q} = \mathbf{0}$  and  $\mathbf{Q} = \kappa_-$  to be most favorable, whose competition further determines the phase diagram within the IVC phase.

We show Hartree-Fock band structures of twisted MoTe<sub>2</sub> at  $\theta = 3.5^\circ$  in Fig. S2 as an example, where we take the same parameters as the soft mode band structures in Fig. 4. For the VP state, the first HF band follows the first non-interacting band of the valley it polarizes to ( $K$  valley in Fig. S2 (a)); while for the IVC state, it hybridizes the first non-interacting band from two valleys. We note a significant magnification of both the band gap and the band width after we introduce interaction. In addition, we also see that the band gap is slightly larger and the band width is narrower in the IVC state since it involves only the lower energy portion of the first band. These features are most obvious in the charge gap plot in Fig. 3 (a) and the renormalized band width plot in Fig. S3 (a). We find a sudden drop of the band width across the VP to IVC transition.

The band structure of the topological VP state and the trivial VP state differ in a more subtle way. Compared to the topological VP state, the trivial VP state deviates from the non-interacting band structure at the  $\kappa_+$  point (see Fig. S2). To understand this behavior, we note that the trivial VP state is closely associated with spontaneous layer polarization (see Fig. S3 (b)) [4, 21]. Interactions will tend to increase layer polarization, and the layer polarized limit is necessarily trivial (in the tight binding limit [4], this is understood as an increased sublattice polarization due to nearest neighbor interactions). Even though the displacement field explicitly breaks the  $C_{2y}$  symmetry that swaps two layers, we still find a sudden increase in layer polarization across the topological to trivial transition up to  $u_D = 10$  meV. At small angles  $\theta \lesssim 1.6^\circ$ , we find spontaneous layer polarization down to zero field.

With the layer polarization picture in mind, we can examine how the interaction mixes the first few bands in detail. As shown in Fig. S4 (b), the  $\kappa_+$  point of the first noninteracting band mainly comes from the top layer, while the rest of the band mainly comes from the bottom layer. On the other hand, the  $\kappa_+$  point of the second band comes from the bottom layer. To polarize the state to the bottom layer, the interaction must mix the first two bands around  $\kappa_+$ . Indeed, as shown in Fig. S4 (a), the covariance matrix  $P^{KK}$  has the highest weight in the first band, except for the  $\kappa_+$  point where the weight is shifted to the second band. Furthermore, the vanishing residue weight on the third band also indicates that it is sufficient to keep only the first two noninteracting bands in this parameter regime.

Finally, we will comment on the effect of including the third band in HF in twisted MoTe<sub>2</sub>. It does not change any of the physics in both the trivial VP phase and the IVC phase, as indicated by the vanishing small weight in Fig. S4 (a). However, in the topological VP phase, it introduces a competing state, which is a layer-unpolarized trivial VP

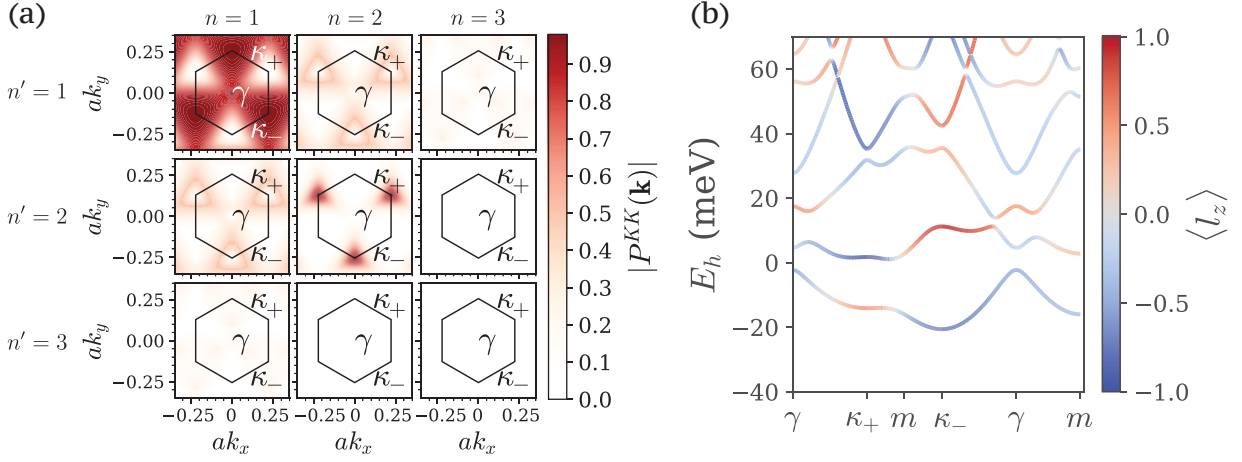


FIG. S4. (a) Nontrivial elements of the one-electron covariance matrix  $[P_0^{\tau'\tau}]^{n'n}(\mathbf{k}) = \delta_{\tau'K} \delta_{\tau K} [P_0^{KK}]^{nn'}(\mathbf{k})$  in the trivial VP phase (polarized to the  $K$  valley). Here we take twisted  $\text{MoTe}_2$  at  $\theta = 3.5^\circ$ ,  $u_D = 5$  meV and  $\epsilon = 10$  in both (a) and (b). (b) Layer polarization of the non-interacting band structure in the  $K$  valley.

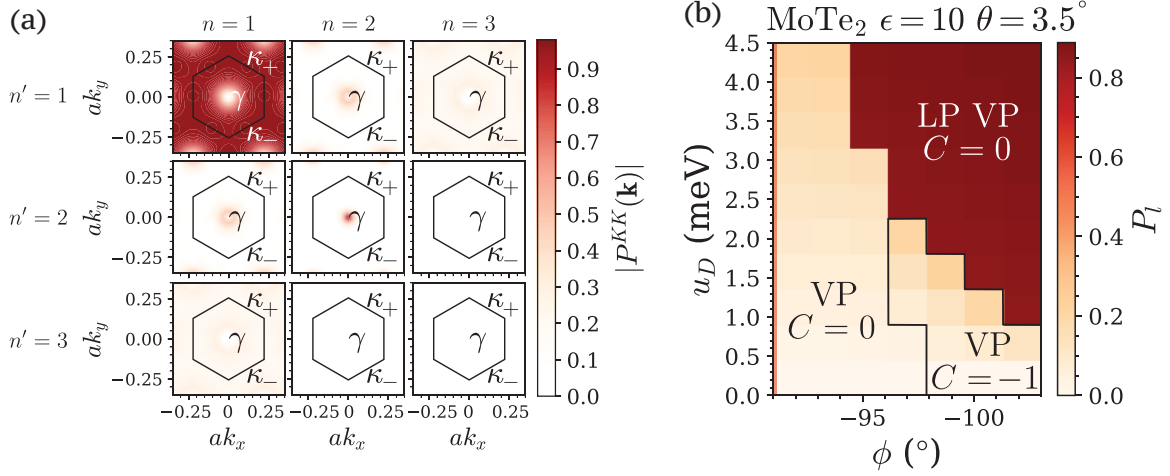


FIG. S5. (a) Nontrivial elements of the one-electron covariance matrix  $[P_0^{\tau'\tau}]^{n'n}(\mathbf{k}) = \delta_{\tau'K} \delta_{\tau K} [P_0^{KK}]^{nn'}(\mathbf{k})$  in the layer-unpolarized trivial VP phase (polarized to the  $K$  valley). Here we take twisted  $\text{MoTe}_2$  at  $\theta = 3.5^\circ$ ,  $u_D = 2$  meV, and  $\epsilon = 10$ . (b) Interacting phase diagram of twisted  $\text{MoTe}_2$  after including three *active* bands as a function of displacement field and the phase  $\phi$  of the moiré potential. We show the layer polarization and label the regime where the ground state has non-zero Chern number. The LP VP  $C = 0$  phase refers to the trivial VP phase discussed in the main text and the VP  $C = 0$  phase is a new phase discussed in Supplementary Material. The  $\phi$  used in the main text is toward the left end of the phase diagram indicated by the red line cut.

state. We note that this is a different state compared to the trivial VP state discussed in the main text, which is always spontaneously layer polarized. We show the covariance matrix  $P^{KK}$  of the layer-unpolarized trivial VP state in Fig. S5 (a), which clearly distinguishes itself from the trivial layer polarized VP (LP VP) state shown in Fig. S4 (a). The interaction mixes the first two bands mainly at the  $\gamma$  point instead of at the  $\kappa_+$  point. The small but non-vanishing weight on the third band also suggests that this state is only favorable when we include three bands in HF. Indeed, if we truncate the covariance matrix to the first two bands and renormalize it, it will have a much higher energy than the topological VP state. However, we note that the competition between this layer-unpolarized trivial VP state and the topological VP state depends sensitively on the continuum model parameters, especially the phase  $\phi$  of the moiré potential in Eqn. S2. As shown in Fig. S4 (b), the topological VP phase is favored at  $|\phi| \gtrsim 96^\circ$ , within the fitting error of the continuous model parameters to the large-scale DFT calculation [4, 29]. We emphasize that the topological VP (QAH) phase has been observed in twisted  $\text{MoTe}_2$  at  $\theta = 3.5^\circ$  and  $\epsilon \sim 10$ , which pinpoints the moiré potential phase  $\phi$  [5, 6]. In the main text, we restrict ourselves to two active bands such that this layer-unpolarized trivial VP state is never favored. We also note that the conclusion of 3 band calculation agrees with that of the full

band calculation.

### SIII. INTERACTION INDUCED MAGNETIC ANISOTROPY

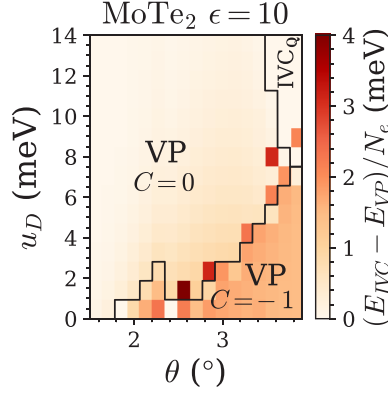


FIG. S6. Energy per particle difference between the  $IVC_0$  and the VP state in twisted  $MoTe_2$ .

In the main text, we discuss the magnetic anisotropy from magnon perspective, characterizing by the Ising anisotropy  $\gamma$ , which drops across the topological transition. Such magnetic anisotropy roots in the energy difference between the VP state and the IVC state as shown in Fig. S6 [43]. We can see that the energy difference closely follows the Ising anisotropy in Fig. 4 (b), including the sudden jump across the topological transition.

### SIV. TOPOLOGICAL TRANSITION AND MAGNETIC CANTING TRANSITION

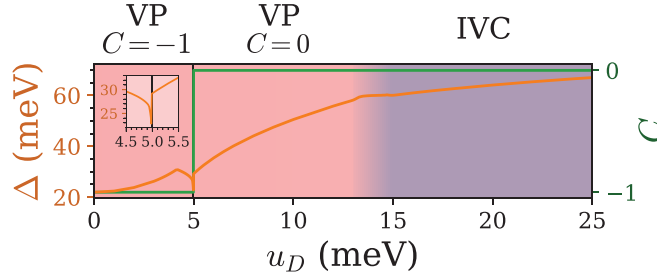


FIG. S7. Typical phase transition as a function of displacement field following the red line cut in Fig. S2 (a) (twisted  $MoTe_2$  at  $\theta = 3.5^\circ$  and  $\epsilon = 10$ ). We show the charge gap  $\Delta$  and the Chern number  $C$  of the first valence band. The inset is a zoom in of the charge gap close to the topological transition.

In this section, we discuss the displacement field-induced transition from the topological VP phase to the trivial VP phase, and eventually to the IVC phase in more detail. In the main text, we present the valley polarization  $P_v$  and the order parameter of  $U(1)_v$  symmetry breaking across the transition (see Fig. 2 (b)). Now we show the Chern number and the charge gap along the same cut in Fig. S7. At  $\epsilon = 10$ , the charge gap develops a deep minimum at the topological transition from the topological VP phase to the trivial VP phase (see the inset of Fig. S7), indicating that it is weakly first order in HF. At larger  $\epsilon$ , this transition is expected to be continuous with the gap going to zero (see, e.g., Ref. 9). Across the magnetic canting transition from the trivial VP phase to the IVC phase, the charge gap never shows any indication of closing, indicating its true continuous nature.

Now we turn our attention to the parameter regime where the intermediate trivial VP is about to vanish. In twisted  $MoTe_2$  at  $\epsilon = 10$ , this happens at  $\theta^c = 3.85^\circ$  and  $u_D = 7.7$  meV. As shown in Fig. S8, the magnetic transition from the trivial VP phase and the IVC phase is always a continuous canting transition up to the critical angle  $\theta^c$ . The weakly first-order topological transition and the continuous magnetic canting transition merge into a first-order transition. Any valley  $U(1)_v$  breaking will be penalized by the topology and, therefore, only shows up in the trivial

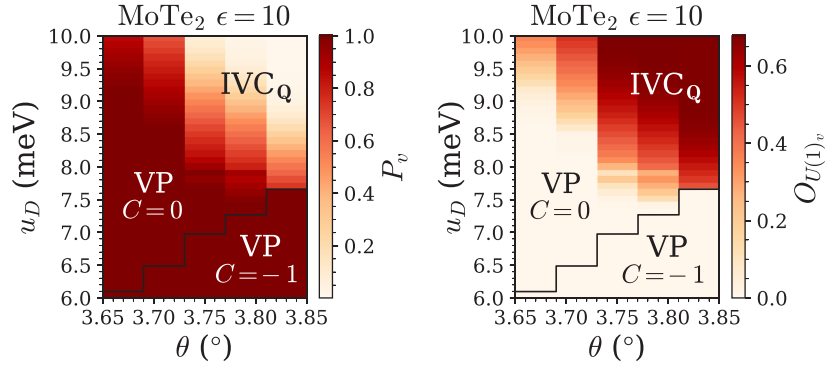


FIG. S8. Interacting phase diagram of twisted MoTe<sub>2</sub> as a function of displacement field and twist angle close to the parameter regime where the intermediate trivial VP vanishes. We show the valley polarization  $P_v$  in (a) and the order parameter of  $U(1)_v$  symmetry breaking in (b).

phase. However, we expect this transition to remain continuous at an even larger  $\epsilon$  where the non-trivial winding of the  $U(1)_v$  order parameter costs less energy.

### SV. SOFT MODES IN THE VP AND THE IVC PHASE

To understand low-energy excitations in these interaction-driven phases, which determine their thermal stability, we use the time-dependent Hartree-Fock calculation to study the eigenmodes of these low-energy excitations and their energetics [26–28]. Following the formulation described in Ref. 25, the starting point is our HF ground state characterized by the covariance matrix  $P(\mathbf{k})$ . We first write down the following ansatz for low energy bosonic excitations characterized by the wavefunction  $[\phi_{\mathbf{q}}^{\tau'\tau}]^{n'n}(\mathbf{k})$ ,

$$\hat{\phi}_{\mathbf{q}} = \sum_{\mathbf{k}} \psi_{n,\tau,\mathbf{k}}^\dagger [\phi_{\mathbf{q}}^{\tau'\tau}]^{n'n}(\mathbf{k}) \psi_{n',\tau',\mathbf{k}+\mathbf{q}} \quad (\text{S7})$$

Now we look for the eigenmodes satisfying

$$\left\langle \left[ \hat{H}, \hat{\phi}_{\mathbf{q}} \right] \right\rangle_{\text{MF}} = \omega_{\mathbf{q}} \hat{\phi}_{\mathbf{q}} \quad (\text{S8})$$

where  $\hat{H}$  is the full interacting Hamiltonian, and  $\langle \cdot \rangle_{\text{MF}}$  means performing partial Wick contractions with the HF ground state  $P(\mathbf{k})$  to reduce all four-fermion operators to two-fermion operators. The eigenmodes can be computed by diagonalizing a quadratic boson Hamiltonian (see Ref. 25 App. A for details). Due to convergence challenges, we restrict ourselves to a  $26 \times 26$  momentum grid for the gapless Goldstone modes in the IVC phase.

To understand the magnon gap in the VP phase (topological or trivial), we can look at the nature of the soft mode at the soft mode bottom. For vast of the phase diagram, the soft mode band bottom appears at  $\mathbf{Q} = \kappa_-$ . We show the wavefunction  $[\phi_{\mathbf{Q}}^{\tau'\tau}]^{n'n}(\mathbf{k})$  of the momentum  $\mathbf{Q}$  soft mode in Fig. S9. The most important character is that it only contains  $\phi^{KK'}$  components, so it indeed corresponds to a magnon instead of an exciton. Condensing such a magnon will give you the IVC<sub>Q</sub> state, which relates the magnon gap to the energy difference between the VP state and the IVC state.

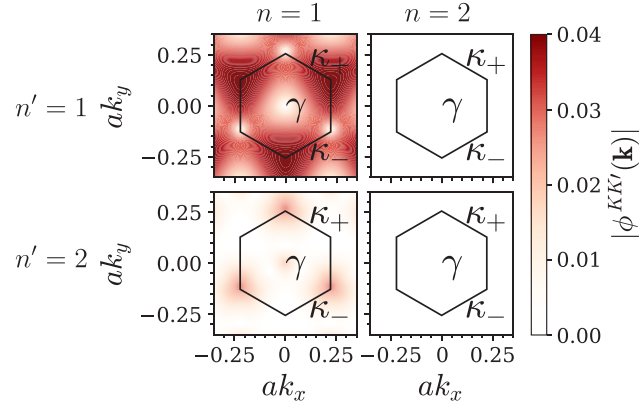


FIG. S9. Nontrivial elements of the momentum  $\mathbf{Q} = \kappa_-$  magnon wavefunction  $[\phi_{\mathbf{Q}}^{\tau\tau}]^{n'n}(\mathbf{k}) = \delta_{\tau'K} \delta_{\tau K'} [\phi_{\mathbf{Q}}^{KK'}]^{nn'}(\mathbf{k})$  in the VP phase (polarized to the  $K$  valley). Here we take twisted  $\text{MoTe}_2$  at  $\theta = 3.5^\circ$  and  $u_D = 1.2 \text{ meV}$  in the topological VP phase as an example.